Nanosized metal clusters

De Hosson, JTM; Palasantzas, G; Vystavel, T; Koch, S

Published in:
JOM

DOI:
10.1007/s11837-004-0271-7

Publication date:
2004

Nanosized Metal Clusters: Challenges and Opportunities

Jeff Th.M. De Hosson, George Palasantzas, Tomas Vystavel, and Siete Koch

This article presents challenges and opportunities to control the microstructure in nanostructured coatings using a nanocluster source. The cluster size distribution is monodisperse and the kinetic energy of the clusters during deposition can be varied. Interestingly, the clusters are grown in extreme non-equilibrium conditions leading to metastable structures of metals and alloys. Because one avoids the effects of nucleation and growth on a specific substrate, one may tailor the properties of the films by choosing the appropriate preparation conditions.

INTRODUCTION

In the microstructure of a nanostructured coating, two key factors determine material strength: the concentration of lattice defects and the details of the numerous interfaces, including the topology of the triple points between the interfaces. The challenge to design a nanostructured coating that is free of defects that degrade the structural and functional behavior. For hard coatings, the key is to avoid grain boundary sliding. For toughness, however, more compliant (amorphous) boundary layers might be more beneficial: Boundary sliding may have a positive effect on wear-resistant coatings by optimizing the ratio of hardness to stiffness.[1,2] Grain boundary sliding seems to limit the further increase in hardness of superhard nanostructured coatings that are mainly used for dry machining tools. Also, Coble creep may occur at the higher temperature of dry machining.[3] Initially, dislocation motion is thought to become suppressed upon grain refinement but softening is expected if grain boundary diffusion dominates over bulk diffusion.

As a rule, all the phases in a nanostructured coating must be made of strong material and the grain boundaries made sharp by optimizing the hardness/stiffness ratio. However, this rule may not always apply. For instance, grain boundary ledges that generate dislocations may become increasingly important in the production of dislocations at smaller grain sizes. When the grain size drops below 20 nm or so in a homogeneous nanostructured material, the number of triple junctions per unit volume becomes appreciably large. Since the triple points possess disclination character, they may contribute substantially to the ductility of nanocomposites and softening is expected at the smallest grain sizes.[1,2] The misorientation across short grain boundaries in nanostructured materials may only be partly accomplished by grain boundary dislocations, and at small sizes the number of disclination dipoles will be increased. Further, crack deflection, crack branching, intergranular fracture, and transgranular fracture are probably much different in these nanostructured materials than in their micrometer-sized counterparts.

In evaluating the performance of a nanostructured coating, it is essential to examine the defect content as well as the microstructural features, namely,[4] grain size dispersion, distribution of interface misorientation angles, and internal strains. Clearly, defects such as microcracks can completely mask the intrinsic strength of the nanostructured coatings. In the past, the low *E*-modulus of nanostructured materials often has been attributed to the unusual grain-boundary structures present, but this phenomenon is actually determined by the defect structure, such as porosity. Further, that control of the grain-size dispersion is extremely important in the experimental design of these coatings. A nanostructured material with a broad grain-size dispersion will exhibit a lower overall flow stress than a material with the same average grain size but with a much smaller grain-size distribution. Consequently, experimental control over the grain-size distribution is important when investigating materials design of nanostructured coatings.

This article presents challenges and opportunities to control the defect content and microstructure in nanostructured coatings via a relatively new approach: using a nanocluster source. An important point is that the cluster size distribution is monodisperse and that the kinetic energy of the clusters during deposition can be varied. Interestingly, the clusters are grown in extreme non-equilibrium conditions that result in metastable structures of metals and alloys. Moreover, because one avoids the effects of nucleation and growth on a specific substrate one may tailor the properties of the films by choosing the appropriate preparation conditions of the preformed clusters.

In general, the crystal structure of nanosized particles depends on temperature and composition. In many cases, the particles have a polyhedral form with various degrees of truncation. These shapes occur due to surface energy minimization for particles formed at equilibrium, or because of kinetics where the shape is determined by the rate at which different crystal faces grow. The combination of factors such as temperature, kinetics, impurities, and surface energy effects could lead also to unusual nanoparticle shapes and size distributions. Therefore, it is crucial to study these controlling factors in detail with high-resolution transmission-electron microscopy (TEM).

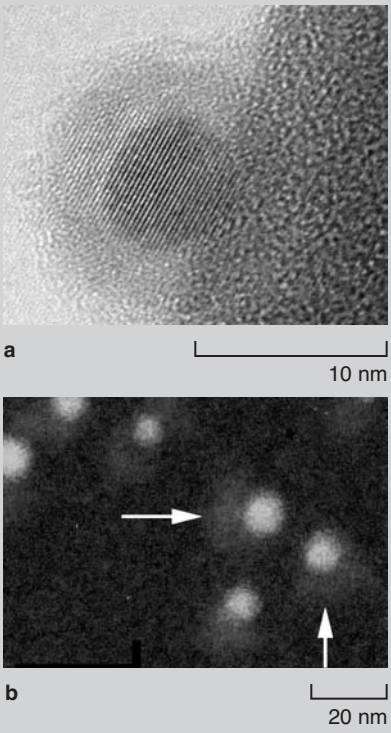

Figure 1. (a) A TEM picture of one iron cluster exposed to air. Lattice fringes correspond with {110} planes of bulk α - iron; (b) elemental mapping using energy-filtered TEM.

NANOCLUSTER SOURCE

In this study, cluster deposition was performed using a NC200U nanocluster source manufactured by Oxford Applied Research.[5] It is based on the gas-aggregation technique developed by Haberland and co-workers,[6] using a magnetron-sputtering device to create an atomic vapor. Briefly, due to collisions with argon atoms, metal atoms lose energy and combine to form clusters, which are subsequently jet-propelled through a nozzle to form a cluster beam. The sputtered atoms combine in a flow of argon at a pressure of $4 \cdot 10^{-2}$ Pa. The chamber base pressure in this study was ~10^{-6} Pa, and the magnetron power was set to ~75 W (300 V and plasma current ~0.25 A).

The morphology and properties of cluster films depend strongly on the cluster impact energy. Generally, three regimes can be distinguished: low energy (~0.1 eV/atom), medium energy (~1–10 eV/atom), and high energy (>10 eV/atom).[7] The low and medium energy deposition produces films with clusters that stay rather intact upon impact. However, these are porous (preserving their high surface-to-volume ratio, which is important for other applications such as catalysis) and weakly adhering films. On the other hand, high-energy deposition may lead to cluster disruption and strong anchoring with the substrate.

In this study, clusters were deposited directly on Si_3Ni_4 and carbon support films with a thickness of 20 nm for TEM analysis.[8] Growth-front aspects of copper nanocluster films deposited with low energy (soft landing films) onto silicon substrates at room temperature were investigated by atomic force microscopy (AFM).[9]

STRUCTURE AND COALESCENCE OF NANOSIZED CLUSTERS

Iron-Based Systems

Studies of nanometer-scale magnetic clusters are of particular interest because of potential applications in high-density magnetic recording media. Because a large fraction of atoms in nanoclusters (~5 nm) are surface atoms, the mechanical, thermal, and magnetic properties[10–12] are quite different from their bulk counterparts. Although many investigations of low-temperature physical properties of magnetic nanoclusters have been performed,[13–19] only a few studies have been conducted on nanosized cluster properties at higher temperatures.[20] The latter are necessary because device operation might lead to heating and alteration of structural components that may affect performance. The challenge is to study the structure of nanometer-sized iron clusters and their response to high temperatures with in-situ TEM experiments.

Transmission-electron microscopy observations showed clearly a uniform cluster size. The TEM analysis of the as-grown clusters indicates that an oxidation process occurs as long as the sample is exposed to air, even during sample transfer from the cluster-source apparatus to the transmission-electron microscope. The typical cluster, shown in Figure 1a, is composed of an iron-oxide shell[21] with a thickness of approximately 2 nm and the iron core with a typical diameter a 5 nm. Based on electron-diffraction studies as well as lattice-spacing measurements of the metallic core, the crystal structure is found to correspond to body-centered cubic (bcc) iron.

However, the original shape of the clusters is altered by the oxide shell formation. Various types of oxide shell can form around the iron clusters. The most abundant form of iron oxide is $\gamma - Fe_2O_3$,[22] while in the present system Fe_3O_4 can not be excluded, either. Indeed, Dupuis et al.[21] studied iron thin films (<100 nm) composed of 2–6 nm diameter clusters and found that 20% of their sample had been converted to both Fe_3O_4 and $\gamma - Fe_2O_3$. The oxidation of iron requires the addition of oxygen to the cluster, which results in an increase of the cluster size. However, the shell of oxide is thermally unstable due to its nanometer-scale thickness (~2 nm) against even moderate cluster annealing at temperatures $T \sim T_{mFe}/3$, in which T_{mFe} is the melting temperature of bulk iron (T_{mFe} = 1,538°C). In-situ TEM annealing at a pressure of ~10^{-2} Pa was performed to study the development of the cluster structure. At 500°C, cluster fusion starts to take place. There is no evidence for surface diffusion of the individual clusters. Figure 1b shows the decomposition of the iron-oxide shell during annealing. No iron-oxide phase is detectable either by elemental mapping or by diffraction studies. Nevertheless, an elemental map of oxygen indicates that it is present beyond the cluster area (Figure 1b). A sample drift during elemental mapping can be excluded as the orientation of the oxygen areas clearly indicates (arrows in Figure 1b). After annealing and

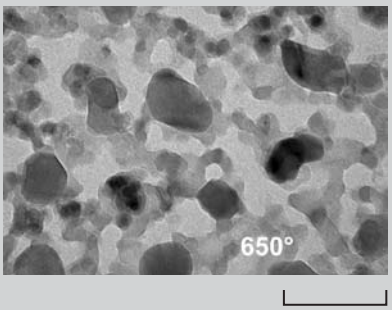

Figure 2. A dense iron nanocluster film at 650°C. At this temperature, nanocluster fusion takes place.

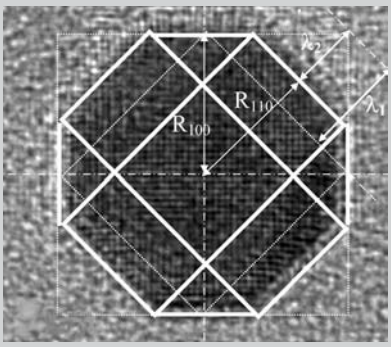

Figure 3. Lattice imaging of an iron nanocluster after in–situ annealing in TEM. The drawings are a <100> projection of truncated rhombic dodecahedron with a schematic explanation of the truncation fraction λ_2 / λ_1.

thermal break up of the oxide shell that surrounds the iron clusters, the crystal structures of the remaining clusters remain bcc. Clusters that are in contact merge to form larger ones (see also Figure 2), while isolated clusters stay intact and are rather immobile.

The most stable structures[23] for medium-sized clusters (100–10,000 atoms) calculated using an empirical many-body potential function are the bcc rhombic dodecahedron with 12 pseudo-close-packed {110} faces (having lowest surface energy for bcc structures,[24] as is supported by calculations using density functional theory[25]), and the icosahedron, which is favorable for smaller clusters. A transition from icosahedron to bcc rhombic dodecahedron is predicted for cluster sizes of approximately 2,000 atoms.[23] Another possibility for stable iron clusters can be cuboctahedron (face-centered-cubic [fcc]) and truncated decahedron,[23] which could be feasible for clusters smaller than those in the present work.

A typical iron cluster observed after the in-situ heating experiments is shown in Figure 3. The actual shape of the cluster is difficult to identify in the case of the <111> projection. In contrast, the shape of the <100> projection (Figure 3) leads clearly to the principal possibility that this shape corresponds to truncated rhombic dodecahedron exposing 12 {110} faces, six {100} faces, and eight {111} faces. The truncation of theoretically envisaged rhombic dodecahedron increases the spherical shape of the cluster although it also increases the fraction of the energetically less favorable faces. The degree of truncation can be described by λ_2/λ_1 (Figure 3) based on the Wulff construction. When $\lambda_2/\lambda_1 = 0$, there is no truncation of the rhombic dodecahedron, while $\lambda_2/\lambda_1 = 1$ represents a fully truncated shape (i.e., a cuboctahedron). An average experimental value of the λ_2/λ_1 fraction is $\lambda_2/\lambda_1 = 0.565 \pm 0.05$, which yields the fraction of surface energies $\gamma_{100}/\gamma_{110} = 1.02$. The ratio between the surface energies can simply be derived from $\lambda_2/\lambda_1 = 2 - \sqrt{2}(\gamma_{100}/\gamma_{110})$ for a rhombic dodecahedron. This result confirms comparable surface energies of {100} and {110} planes found by quantum mechanical calculations.[25] Structural characteristics of reformed clusters (either isolated or generated by fusion of other clusters) differ from former theoretical predictions regarding calculations of stable structural forms since the results of this study favor truncated polyhedron for relatively large cluster sizes. The theoretical calculations concern static properties at 0 K of free clusters, ignoring temperature effects and cluster dynamics.[23]

Niobium-Based Systems

Niobium is used as an example of cluster coalescence because it is a nonmagnetic transition metal and offers relative simplicity in the relationship between structure and functional cluster properties. Niobium atoms form strong directional chemical bonds that lead to well-defined structures. The majority of studies on niobium clusters thus far have focused on systems with a rather small number of atoms per cluster (<30), their special physical properties (ionization potential, electron affinity, and atomization energy as a function of cluster size),[26,27] and structural properties.[28] Research on the dynamic aspects of larger niobium clusters as a function of temperature has been very limited. It has been suggested that niobium nanoparticles possess a truncated rhombic dodecahedron crystal.[29] The authors explored the crystallography of nanometer-scale niobium clusters, in addition to any cluster-cluster interactions and structural transitions that might occur under in-situ heat treatment up to a temperature of 800°C.

To ensure that the niobium remained intact with a bcc structure, as diffraction analysis indicated, deposition occurred at room temperature and at low energy. No oxide shell was detectable as in the previous case of iron clusters, and the deposited clusters did not collapse or exhibit structural instabilities under electron-beam irradiation. The temperature of 800°C is the highest that the Si_3N_4 substrate can withstand.

As is shown in diffraction analysis, considerable structural changes occur as a result of the heat treatment. The first, detectable at 300°C, is the slight shift of the 110 peak. The maximum shift is observed at 500°C, where the shift represents an expansion of the lattice parameter by approximately 7%, which is at the initial stage of the bcc-to-fcc structural transformation. The structural changes are due to oxidation of the clusters, with NbO (cubic monoxide) to be the most likely structure since it is known to form under low oxygen pressure.[30] This is typical for the ambient vacuum of ~10^{-7} Torr during in-situ heat treatment inside the TEM. In addition, the electron energy loss spectroscopy (EELS) performed after annealing shows clearly the presence of the oxygen in an analyzed area, leaving no doubt of the formation of niobium oxide.

The crystal structure at room temperature, shown by the <111> projection having a hexagonal shape, corresponds to a rhombic dodecahedron, while hexagonal <110> and square <100> projections were also found. The case of untruncated dodecahedron yields surface energies of $\gamma_{100}/\gamma_{110} \geq \sqrt{2}$, and

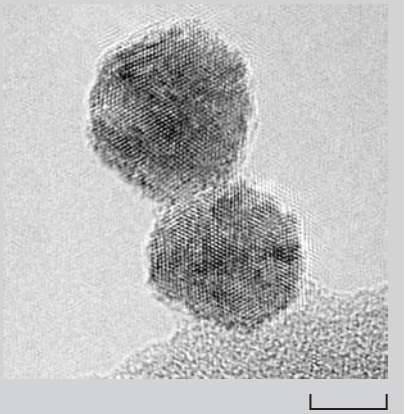

Figure 4. Two niobium nanoclusters after heat treatment at 800°C; no coalescence is observed.

this is in agreement with the fact that the {110} faces have the lowest surface energy for bcc structures.[24]

Figure 4 illustrates that cluster coalescence events were not observed even at rather elevated temperatures of $T \cong T_M/3$ (with T_M = 2,750 K and T_M = 2,210 K, the melting temperatures of bulk niobium and NbO, respectively),[31] although the melting temperature of clusters will be lower than T_M due to its dependence on cluster diameter.[32,33] The driving force for coalescence is the diffusion of atoms on the cluster surface from the regions of high curvature (where they have fewer neighbors and therefore are less strongly bound) toward the regions of lower curvature. The absence of coalescence supports the hypothesis that the cluster melting temperature is close to the bulk value. Long coalescence times have also been attributed to the presence of facets on the initial cluster surface that persist and rearrange during coalescence.[34]

Indeed, for faceted nanosized clusters, the diffusion of surface atoms has been observed to be slow even at temperatures 200°C below the melting point, allowing very few atoms to move a significant distance away from the contact region. Experiments have shown that shape evolution is very slow in the presence of facets for three-dimensional crystallites.[35] Both experiments[36] and computer simulations[35] on two-dimensional islands suggest that the presence of facets can be effective in slowing down the coalescence process. More work is underway to get a quantitative understanding of nanoparticle coalescence by including crystalline anisotropy in the surface diffusion theory of Mullins and Nichols.[37]

Comparison of Iron and Niobium

When comparing nanosized clusters of niobium and iron (both corresponding to a bcc system) prepared with the same source under identical conditions, the as-deposited iron clusters were enclosed by an oxide shell of thickness ~2 nm while, for niobium, any oxide shell is undetectable with oxidation occurring upon further heat treatments at elevated temperatures. Indeed, upon heat treatment up to temperatures as high as $T_m/3$, the iron cluster coalescence was fast with the clusters fully fused into larger ones. After disintegration of the oxide, the crystal habit of the annealed iron nanosized clusters was a truncated rhombic dodecahedron. Nevertheless, no significant change was observed in niobium cluster size after heat treatment. Indeed, even if the whole cluster was oxidized forming NbO, since for the niobium and NbO the volume per atom is $1.808 \cdot 10^{-2}$ nm^3 and $2.541 \cdot 10^{-2}$ nm^3, respectively, that would lead to a size of $D_{NbO}/d_{Nb} \approx 1.12$. The latter yields an increment in size of, at most, 12%, which could be observed by high-resolution TEM. However, the presence of the delocalization effect around the cluster edges can hide small size increments of the order of 10%.[38]

GROWTH OF NANOSIZED CLUSTER FILMS

Few studies have explicitly considered scaling aspects of the surface morphology for nanosized cluster films and their relation to microscopic film growth mechanisms. Moseler et al.[39] reported an Edwards-Wilkinson type of growth for highly energetic (~5 eV/atom) copper clusters onto silicon. Growth studies for low-energy (<0.5 eV/atom) deposited carbon clusters on silicon and copper by Buzio et al.,[40] using AFM, yielded roughness and growth exponents of, respectively, H = 0.64–0.68 and β = 0.42–0.50 (largely independent on the average cluster size, although the presence of large particles within the cluster beam induced significant morphology fluctuations). For carbon particles the covalent bonding prohibits cluster coalescence.

This example provides an analysis of low-energy copper nanosized cluster deposition with a narrow size distribution. The film surface morphology was characterized in air (relative humidity ~45%) using a Digital Instruments Dimension 3100 AFM, which was operated in tapping mode[41] to minimize damage of the film surface. The cantilever oscillation amplitude was maintained by a feedback loop with a set-point value of ~1.0 V. Clusters could be attached to the tip resulting in distorted images due to multiple-tip effects. Image reproducibility was verified by repeated scans over the same area to exclude any tip effects. The AFM tip and cantilever are an integrated assembly of single-crystal silicon (produced by etching). The tip radius is ≤10 nm with a side angle of ≤10°. Transmission electron microscopy on simultaneously exposed Si_3N_4 membrane substrates revealed a supported cluster size of the order of 10 nm, comparable to the AFM tip radius. Although isolated clusters can be resolved with AFM, tip convolution has a significant influence on the observed lateral size of such clusters.[42]

Upon impingement of copper clusters on the silicon substrate, cluster coalescence and partial submersion into the substrate surface occur. Figure 5 is a deflection image that shows the change of the cantilever deflection amplitude recorded simultaneously with the height data. The time τ can be estimated for two spheres of radius R_{Cu} to coalesce and form one sphere by grain boundary diffusion as $\tau = [A(k_BT)/V_m\gamma_{Cu}(\delta D)]R_{Cu}^4(X/R_{Cu})^6$,[43] in which $A = 0.0125$, $V_m \approx 9.1 \times 10^{-30}$ m^3 represents the volume of one copper atom, $\gamma_{Cu} = 1.75$ J/m^2 is the surface energy of copper (for Cu (001)), and $(\delta D) = 2 \times 10^{-14} \exp(-105$ kJmol^{-1}/RT) m^3/s is the grain boundary diffusivity of copper, and δ is the interface width along which diffusion occurs.[44] The factor (X/R) is the ratio between the neck size and the cluster radius. In the initial stage with a small X/R, such as 0.1, $\tau \cong 0.25$ s at room temperature for R_{Cu} = 5 nm. Therefore, such a process occurs reasonably quickly during cluster deposition. Furthermore, the presence of a rim around the clusters (see Figure 5) indicates a partial submersion into the substrate, whereby

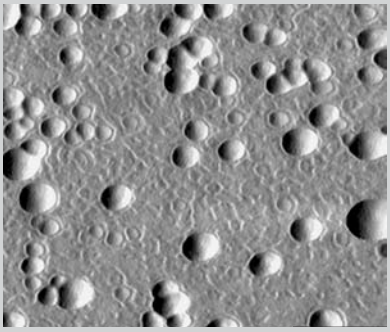

Figure 5. An AFM deflection image (scan size 1 μm) of an open copper nanocluster film showing partial submersion into the silicon surface.

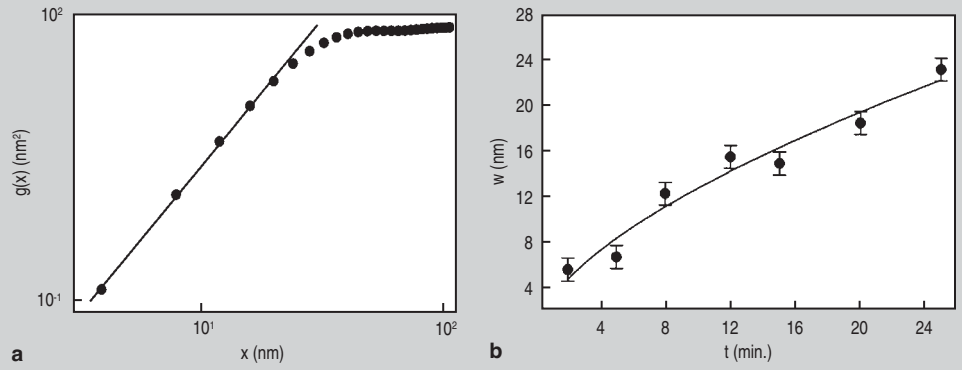

Figure 6. The height-difference correlation function vs. lateral scale x. The actual scan size in the measurement of g(x) is 2 μm. The linear fit yields the roughness exponent H = 0.49 ± 0.03. The saturation regime is w = 6.7 nm, and the correlation length is ξ = 31 nm, which is comparable with the average particle size in (a), the AFM image (scan size 500 nm). (b) shows that the rms roughness amplitude w grows as a power law with deposition time t. The fit yields an exponent β = 0.61 ± 0.07.

clusters are partly covered by substrate material. This can be explained by the higher surface energy of copper than that of silicon ($\gamma_{Si} = 1.4\ J/m^2$).[45] Submergence is driven by large capillary forces on the clusters, and it occurs if the cluster has sufficient kinetic energy and significantly higher surface energy than the substrate.[46]

For each film, the height-difference correlation function $g(x) = \langle [h(x) - h(0)]^2 \rangle$ in the fast scan direction was computed, with h(x) the surface height at lateral position x ($\langle h(x) \rangle = 0$). The results were averaged over five AFM topography images (with 512 points/line scan) acquired at different locations on the film surface (Figure 6). For a self-affine rough morphology, $g(x) = \rho^2 x^{2H}$ for $x << \xi$ and $g(x) = 2w^2$ for $x >> \xi$ (with ξ the lateral correlation length and $\rho \propto w / \xi^H$ the average local surface slope). The rms roughness amplitude w can be obtained from the saturated regime of g(x), while a double log-plot at shorter length scales yields the roughness exponent H. As H decreases, the surface becomes more irregular (jagged) at short length scales ($x << \xi$).[47] Finally, the intersection of power-law and saturation lines gives the correlation length $\xi = (2w^2 / \rho^2)^{1/2H}$.

The height distribution P(h) shows deviations from pure Gaussian behavior. To quantify this point further, the authors calculated the skewness $S = \int h^3 [P(h) / \int P(h) dh] dh / w^3$, which is a measure of the distribution symmetry around a reference surface level. For a Gaussian distribution S = 0, while in the present case for all film thicknesses of S > 0, indicating that the $h \leftrightarrow -h$ symmetry is broken. This can be attributed to a non-linearity associated with the dependence of growth on the local surface inclination.[48]

The growth of the rms amplitude w is quantified by the growth exponent $\beta = 0.62 \pm 0.07$ as $w \sim t^{\beta}$ (see Figure 6b).[49] The roughness exponent H was found to be $H = 0.45 \pm 0.05$. The average local surface slope ρ ($\propto w / \xi^H$) increases with deposition time as a power law $\rho \propto t^c$ with $c = 0.73 \pm 0.09$, which is even more evidence of surface roughening. Although the rms amplitude w increases with growth time, the correlation length ξ saturates to a value ~34–40 nm for later stages of growth, indicating the development of limited lateral correlations.

Due to the influence of the finite AFM tip curvature, the actual roughness exponents H might be slightly smaller than the obtained values of $H = 0.45 \pm 0.05$,[50] but they appear to be close to that predicted by the KPZ (Kardar-Parisi-Zhang) model, $H \approx 0.4$.[51,52] In this model the dominant relaxation mechanisms are desorption or the formation of pores.[48] However, the different growth exponent ($\beta \approx 0.62$) than that of the KPZ scenario ($\beta_{KPZ} \approx 0.25$) can be attributed to local diffusion processes that eventually lead to cluster coalescence.

Surface diffusion of deposited clusters (as a whole) would result in a different roughness exponent (i.e., $H > 0.6$).[53,54] Moreover, during early deposition stages (prior to film closure) the diffusion coefficient of a deposited cluster scales with the size or number of atoms n within the cluster as $D_n = D_1 / n^c$ ($c > 0$).[55] This will lead to very small diffusion coefficients ($D_n << D_1$) for clusters much larger than 10 nm. In fact, for $c = 0.3–1.7$ and $n \approx 3.6 \cdot 10^5$ (for cluster diameter 10 nm), the ratio can be estimated at $D_n / D_1 \cong 0.02$, which excludes the diffusion of entire copper clusters to play a predominant role as a surface relaxation mechanism.

The asymmetrical height distribution and the measured scaling exponents indicate a complex non-linear roughening mechanism, dominated by porosity. The film-growth mode has similarities with the KPZ scenario, where a deposited cluster becomes part of the aggregate when it meets another cluster. However, it appears that subsequent local cluster coalescence effects cause deviations from a pure KPZ type of growth. The fact that the low-energy deposited films may have a significant porous structure is also revealed by mechanical nanoindentation tests (Figure 7). The hardness and modulus values lie below those of solid copper. Clearly, these findings are related to the internal film structure, which is of significant complexity. Analysis by TEM indicates that the deposited clusters might be composed of sub-grains (see Figure 7b).

CHALLENGES AND OPPORTUNITIES

An interesting route for future research is to explore the energy of deposition as an experimental parameter. High-impact energy deposition has been more than a shining success in producing exceptionally good (smooth and highly adhering) coatings.[56] This is because diffusion and local rapid annealing of the constituent atoms follow cluster fragmentation. As a consequence, hills and valleys are removed, producing very smooth films. Moreover, the cluster fragmentation enhances the formation of nucleation sites and adatom diffusion, allowing the formation of epitaxial coatings at room temperature despite a 25% lattice misfit (i.e., Al/Si(111)).[57]

Besides these more or less granular structures of nanosized grains in the design part of nanocomposite coatings, one can also change the dimensionality in the system, (e.g., a significant enhancement of the mechanical stability can be expected in nanostructured multilayers with different chemical

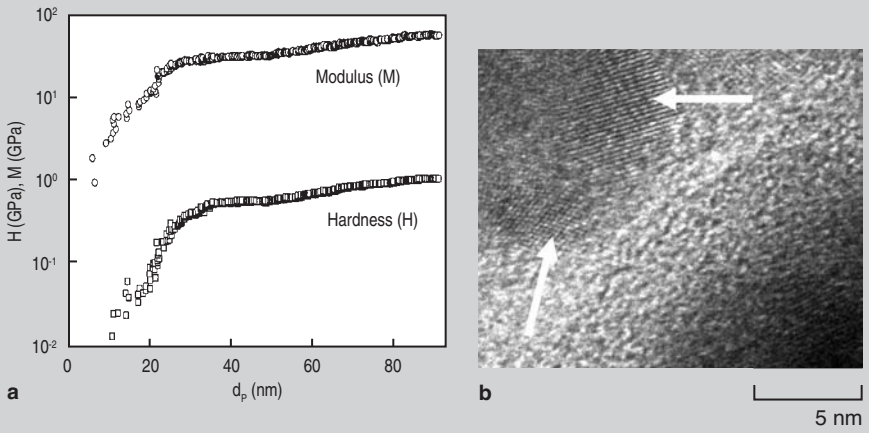

Figure 7. (a) The nanoindentation measurement of hardness and modulus for a 110 nm thick copper film as a function of nanoindentor penetration depth. (b) A high-resolution TEM image where arrows indicate within a cluster the presence of different crystallographic orientations suggesting a sub-grain polycrystalline structure.

compositions). The design parameters are the wavelength of the compositional modulation and amplitude. At smaller wavelengths (several nanometers), coherence strain effects may dominate the hardness increase rather than the image forces of dislocations, which become partially cancelled across the interfaces between very thin layers or do not exist because of the dislocation line tension problem. The authors contend that the physical idea of long-range stress fields of dislocations should be dropped at these dimensions. This aspect provides interesting opportunities for challenging theoretical and experimental research. In nanocluster deposition, multilayers with and without a graded structure in the direction perpendicular to the surface can be produced and offer largely unexplored areas.

ACKNOWLEDGEMENTS

The authors acknowledge financial support from the Materials Science Center and the Netherlands Institute for Metals Research.

References

1. I.A. Ovid'ko, *Science,* 295 (2002), p. 2386.
2. M.Yu. Gutkin, I.A. Ovid'ko, and C.S. Pande, *Nanoclusters and Nanocrystals,* ed. H.S. Nalwa (Stevenson Ranch, California: Amer. Sci. Pub., 2003), p. 255.
3. S. Veprek and Ali S. Argon, *Journal of Vacuum Science Technology B,* 20 (2002), p. 650.
4. K.J. Van Vliet et al., *Phys. Rev. B,* 67 (2003), p. 104,105; and J.R. Weertman et al., *MRS Bulletin*, 24 (1999), p. 44.
5. H. Haberland et al., *Surface Review and Letters,* 3 (1996), pp. 887–890.
6. C.G. Granqvist and R.A. Buhrman, *Journal of Applied Physics,* 47 (1976), pp. 2200–2219.
7. For main reviews in the field see also: C. Binns, *Surface Science Rep,* 44 (2001), p. 1; W. Eberhardt, *Surface Science,* 500 (2002), p. 242; P. Jenssen, *Review of Modern Physics,* 71 (1999), p. 1695; P. Melinon et al., *Int. Journal of Modern Physics B,* 9 (1995), p. 339.
8. T. Vystavel et al., *Applied Physics Letters,* 82 (2003), pp. 197–200.
9. G. Palasantzas, S.A. Koch, and J.Th.M. De Hosson, *Applied Physics Letters,* 81 (2002), p. 1089.
10. D. Yao et al., *Nanostructured Materials,* 6 (1995), pp. 933–936.
11. Y.Y. Chen et al., *Physical Review Letters,* 84 (200), pp. 4990–4993.
12. J.F. Löffler, H.-B. Braun, and W. Wagner, *Physical Review Letters,* 85 (2000), pp. 1990–1993.
13. C. Binns et al., *physica status solidi (a),* 189 (2002), pp. 339–350.
14. S. Gangopadhyay et al., *Journal of Applied Physics,* 70 (1991), pp. 5888–5890.
15. W. Gong et al., *Journal of Applied Physics,* 69 (1991), pp. 5119–5121.
16. S. Gangopadhyay et al., *Physical Review B,* 45 (1992), pp. 9778–9787.
17. S. Gangopadhyay et al., *Journal of Applied Physics,* 73 (1993), pp. 6964–6966.
18. F. Bødker, S. Mørup, and S. Linderoth, *Physical Review Letters,* 72 (1994), pp. 282–285.
19. M. Holdenried, B. Hackenbroich, and H. Micklitz, *Journal of Magnetism and Magnetic Materials,* 231 (2001), pp. L13–L19.
20. Y.D. Yao et al., *Nanostructured Materials,* 6 (1995), pp. 933–936.
21. V. Dupuis et al., *Journal of Applied Physics,* 76 (1994), pp. 6676–6678.
22. M.D. Upward et al., *Journal of Vacuum Science & Technology B,* 18 (2000), pp. 2646–2649.
23. N.A. Besley et al., *Journal of Molecular Structure (THEOCHEM),* 341 (1995), pp. 75–90.
24. D. Wolf, *Philosophical Magazine A,* 63 (1991), pp. 337–361.
25. M.J.S. Spencer et al., *Surface Science,* 513 (2002), pp. 389–398.
26. J. Zhao, X. Chen, and G. Wang, *Physics Letters A,* 214 (1996), pp. 211–214.
27. A. Berces et al., *Journal of Chemical Physics,* 108 (1998), pp. 5476–5490.
28. V. Kumar and Y. Kawazoe, *Physical Review B,* 65 (2002), p. 125403.
29. A.S. Edelstein and R.C. Cammarata, editors, *Nanomaterials: Synthesis, Properties and Application* (Bristol, U.K.: Institute of Physics Publishing, 1998).
30. M. Petrucci et al., *Journal of Applied Physics,* 63 (1988), pp. 900–909.
31. J.E. Macintyre, editor, *Dictionary of Inorganic Compounds,* volumes 1–3 (London: Chapman & Hall, 1992).
32. P. Buffat and J.-P. Borel, *Physical Review A,* 13 (1976), pp. 2287–2298.
33. M. Schmidt and H. Haberland, *Comptes Rendus Physique,* 3 (2002), pp. 327–340.
34. L.J. Lewis, P. Jensen, and J.-L. Barrat, *Physical Review B,* 56 (1997), pp. 2248–2257.
35. P. Jensen, *Reviews of Modern Physics,* 71 (1999), pp. 1695–1735.
36. C.R. Stoldt et al., *Physical Review Letters,* 81 (1998), pp. 2950–2953.
37. F.A. Nichols and W.W. Mullins, *Journal of Applied Physics,* 36 (1965), p. 1826.
38. T. Vystavel et al., *Applied Physics Letters,* 83 (2003), p. 9309.
39. M. Moseler et al., *Nuclear Instruments and Methods in Physics Research B,* 164–165 (2000), p. 522.
40. R. Buzio et al., *Surface Science,* 444 (2000), p. L1.
41. D. Sarid, *Scanning Force Microscopy with Applications to Electric, Magnetic and Atomic Forces,* Revised Edition (New York: Oxford University Press, 1994).
42. G.L. Hornyak et al., *Micron,* 29 (1998), p. 183.
43. R.M. German, *Sintering Theory and Practice* (New York: Wiley, 1996), p. 100.
44. A.P. Sutton and R.W. Balluffi, *Interfaces in Crystalline Materials* (New York: Oxford University Press, 1995), pp. 792–793.
45. D.J. Eaglesham et al., *Physics Review Letters,* 70 (1993), p. 1643.
46. C.G. Zimmermann et al., *Physics Review Letters,* 83 (1999), p. 1163.
47. Y.P. Zhao, G.-C. Wang, and T.-M. Lu, *Experimental Methods in the Physical Science: Vol. 37—Characterization of Amorphous and Crystalline Rough Surfaces-Principles and Applications* (New York: Academic Press, 2000).
48. P. Meakin, *Fractals, Scaling, and Growth Far from Equilibrium* (Cambridge, U.K.: Cambridge University Press, 1998).
49. J. Krim and G. Palasantzas, *Int. Journal of Modern Physics B,* 9 (1995), p. 599.
50. J.-J Aué and J.Th.M. De Hosson, *Applied Physics Letters,* 71 (1997), p. 1347.
51. M. Kardar, G. Parisi, and Y.C. Zhang, *Physics Review Letters,* 56 (1986), p. 889.
52. T. Halpin-Heally, *Physics Rep.,* 254 (1995), p. 215; M. Forest and L.–H. Tang, *Physics Review Letters,* 64 (1991), p. 1405.
53. W.E. Wolf and J. Villain, *Europhysics Letters,* 13 (1990), p. 389.
54. Z.-W. Lai and S. Das Sarma, *Physics Review Letters,* 66 (1991), p. 2348.
55. D. Kashchiev, *Surface Science,* 55 (1976), p. 477; B. Lewis, *Surface Science,* 21 (1970), p. 289.
56. H. Haberland et al., *Journal of Vacuum Science Technology A,* 10 (1992), p. 3266; H. Haberland et al., *Nuclear Instruments & Methods Physics Research Section B,* 80/81 (1993), p. 1320.
57. I. Yamada, *Nuclear Instruments & Methods B,* 55 (1991), p. 544.

Jeff Th.M. De Hosson is a professor, George Palasantzas is a scientific staff member and lecturer, Tomas Vystavel is a post doctorate, and Siete Koch is a Ph.D. student with the Department of Applied Physics at the University of Groningen in the Netherlands.

For more information, contact Jeff Th.M. De Hosson, University of Groningen, Department of Applied Physics, Materials Science Center and Netherlands Institute for Metals Research, Nijenborgh 4, 9747 AG Groningen, The Netherlands; +31-503-63-4898; fax +31-503-63-4881; e-mail hossonj@phys.rug.nl.